2013

In vitro evaluation of PEGylated mesoporous MgFe2O4 magnetic nanoassemblies (MMNs) for chemo-thermal therapy

Sunil Kumar
Indian Institute of Technology Bombay

Amita Daverey
Indian Institute of Technology Bombay

Niroj Kumar Sahu
Indian Institute of Technology Bombay

Dhirendra Bahadur
Indian Institute of Technology Bombay, dhirenb@iitb.ac.in

Journal of Materials Chemistry B

RSC Publishing

PAPER

View Article Online
View Journal | View Issue

In vitro evaluation of PEGylated mesoporous $MgFe_2O_4$ magnetic nanoassemblies (MMNs) for chemo-thermal therapy†

Cite this: *J. Mater. Chem. B*, 2013, **1**, 3652

Sunil Kumar,[a] Amita Daverey,‡[b] Niroj Kumar Sahu[b] and Dhirendra Bahadur*[b]

Received 26th March 2013
Accepted 20th May 2013

DOI: 10.1039/c3tb20429d

www.rsc.org/MaterialsB

A size tunable synthesis of mesoporous $MgFe_2O_4$ magnetic nanoassemblies (MMNs) through a PEG-diacid mediated polyol method is reported. The PEG-diacid coated MMNs exhibit a significant specific surface area of 92 m^2 g^{-1} and saturation magnetization of 57 emu g^{-1}. These MMNs exhibit a very good colloidal stability in PBS (pH 7.4) with nonappreciable cytotoxicity in mouse fibroblast (L929) and cervical cancer (HeLa) cells. We demonstrate the potential of MMNs as an integrated nanosystem for drug delivery and magnetic hyperthermia (MHT) through *in vitro* studies. 80% loading efficiency of doxorubicin (DOX) has been achieved due to the highly negative surface charge and mesoporous nature of MMNs. It is observed that 65–70% of HeLa cells undergo apoptosis through DNA fragmentation after 24 h of incubation with DOX loaded MMNs. MHT alone induces the death of 40–45% of cells, whereas the synergistic effect of a combination of DOX and MHT leads to the death of about 90% of cells. Our results show that MHT significantly increases the therapeutic efficacy of DOX to induce more apoptosis in cancer cells. Hence, a combination of MHT with chemotherapy makes MMNs a powerful multimodal system for synergistic chemo-thermal cancer therapy.

1 Introduction

Chemotherapy is the first line therapy for the treatment of cancer. But several disadvantages associated with this therapy such as nonselective distribution of drugs, multidrug resistance, undesirable side effects on normal tissue and other physical inconveniences to the patients resulted in researchers developing alternative approaches for the improved treatment of cancer. Nano drug-delivery systems have been shown to reduce some side effects of chemotherapy associated with nonselective distribution and the toxic effects of drugs.[1,2] Besides delivery of the drug to the tumour sites, advanced nanomaterials have been shown to open doors to dual-therapies. Moving in this direction, nanomaterials having the functionalities of hyperthermia and chemotherapy in a single system are more in demand for cancer treatment. Several studies have shown that the therapeutic efficacy of any anticancer drug such as doxorubicin (DOX) can be enhanced by combination with hyperthermia.[3,4] Different nanostructures such as gold nano shells,[5] carbon nanotubes,[6] graphene,[7] and magnetic nanoparticles[3,8] have been used extensively for the chemo-thermal ablation of tumours. Among these, oxide magnetic nanoparticles (MNPs) have emerged as a better option due to their good biocompatibility, degradability under mild acidic conditions, magnetic manipulation, magnetic resonance imaging (MRI) properties and capability to generate controlled non-invasive heat under an alternating current (AC) magnetic field (AMF).[8–10] MNPs have been used for several drug delivery applications, but one of the limitations is their ability to carry a large amount of anticancer drug at tumour sites. To enhance the drug carrying capacity of MNPs, various nanohybrid drug delivery carriers such as peptide mimic shell cross-linked magnetic nanocarriers (PMNCs),[11] magnetic liposomes,[8] alginate embedded magnetic nanoheaters[3] *etc.* have been developed. However, these nanohybrids also have problems such as large size, complex design and non-reproducibility. Recently, mesoporous[12] and hollow nanoparticles[13] have emerged as promising candidates for dual therapy due to their capability to hold a large amount of anticancer drug at the tumour site and minimize systemic drug toxicity. These features of mesoporous nanoparticles are attributed to their large surface area and pore volume.[12] Previous studies have reported the synthesis of water dispersible mesoporous magnetic nanoassemblies (MMNs) using polyacrylic acid,[14] trisodium citrate,[15] and poly-γ-glutamic acid[12] as stabilizing agents. However, these methods have their limitations with respect to

[a]*Department of Chemical Engineering, Indian Institute of Technology Bombay, Mumbai-400076, India*

[b]*Department of Metallurgical Engineering and Materials Science, Indian Institute of Technology Bombay, Mumbai-400076, India. E-mail: dhirenb@iitb.ac.in; Fax: +91 22 2576 3480; Tel: +91 22 25767632*

† Electronic supplementary information (ESI) available: TEM, SEM, XRD, porosimetry, magnetization data, cell biocompatibility study *etc.* are described. See DOI: 10.1039/c3tb20429d

‡ Present address: Department of Chemical and Biomolecular Engineering, University of Nebraska, Lincoln, NE-68588. USA.

biocompatibility or the large size of the magnetic nanoassemblies (>200 nm). Large nanoassemblies cannot be efficiently injected into the body intravenously as a drug carrier. In addition, due to large size of the particles, they are easily sequestered by the spleen and removed by the phagocyte system of the body resulting in the reduction of blood circulation time.[16,17] Therefore, new methods and suitable stabilizing agents are needed to synthesize ideal magnetic nanoassemblies uniquely capable of drug delivery, imaging and magnetic hyperthermia.

In the present work, we have prepared a novel, highly water dispersible, biocompatible and size tunable (<100 nm) mesoporous $MgFe_2O_4$ magnetic nanoassemblies (MMNs) by a polyol method using PEG-diacid as a stabilizing agent. The advantages of the synthesized MMNs over other nanoassemblies and nanoparticles are (i) their size range lies between the renal clearance threshold (~8 nm) and the gap in leaky cancer blood vessels (~100 nm), which is good to exploit passive tumour targeting through enhanced permeation and retention effect (EPR),[16] (ii) PEG modification on the surface of the MMNs helps in resisting the adsorption of unwanted plasma protein and increases the colloidal stability for prolonged blood circulation, and (iii) MMNs are more biocompatible due to the presence of Mg^{2+} ions which are required for ATP hydrolysis for energy generation, genomic stability and catalytic activity of almost all enzymatic systems involved in DNA processing.[18,19] The potential applications of these MMNs were evaluated for DOX delivery and magnetic hyperthermia (Scheme 1). DOX was loaded into mesoporous MMNs through electrostatic interaction, henceforth referred to in the text as DOX–MMNs. We compared the combined effect of chemotherapy and MHT with individual treatments in human cervix adenocarcinoma HeLa cells. Our results show the novelty and potential of DOX–MMNs for synergistic combination therapy leading to apoptosis through DNA fragmentation and cell membrane distortion. The enhancement of the DOX efficacy and the synergistic effect with MHT to induce more cell death make MMNs a powerful nanosystem for chemo-thermal cancer therapy.

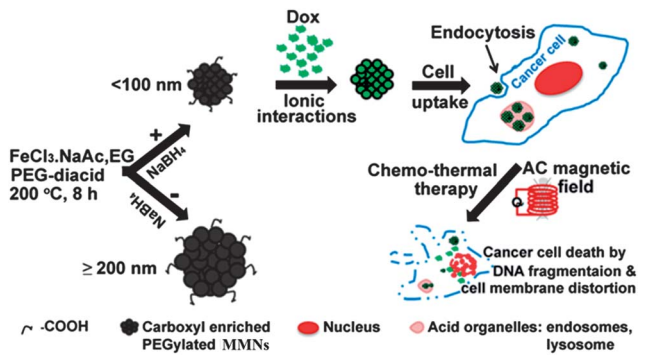

Scheme 1 Schematic representation of carboxyl enriched PEGylated MMNs synthesis and evaluation of their efficiency for chemo-thermal treatment against cancer cells.

2 Experimental section

2.1 Reagents and materials

All the chemicals were of analytical grade and used as received. Iron(III) chloride hexahydrate ($FeCl_3 \cdot 6H_2O$, 99%), magnesium(II) chloride hexahydrate ($MgCl_2 \cdot 6H_2O$, 99%), doxorubicin–HCl salt (DOX, ≥98%), poly(ethylene glycol)bis(carboxy methyl) ether (HOOC–PEG–COOH Mn 600), 3-(4,5-dimethyl-thiazol-2yl)-2,5-diphenyl tetrazolium bromide (MTT, >98%), 4,6-diamidino-2-phenylindole (DAPI, >98%), propidium iodide (PI, >94%), ethidium bromide (EtBr, >95%), and rhodamine-6G (99%) and phalloidin-tetramethyl rhodamine-B-isothiocyanate conjugates were purchased from Sigma-Aldrich Co. (St. Louis, MO, USA). 3-(4,5-dimethylthiazol-2-yl)-5-(3-carboxymethoxyphenyl)-2-(4-sulfophenyl)-2*H*-tetrazolium (inner salts, MTS) and phenazine methoxysulfonate were procured from Promega (PMS), Madison, USA. Sodium borohydride ($NaBH_4$, Merck, 98%), sodium acetate (CH_3COONa, Aldrich, 99%) and ethylene glycol (EG, Merck, 99.8%) were used in the reaction. Dulbecco's modified eagle medium (DMEM), antibiotic and antimycotic solution were obtained from Hi-Media Ltd (Mumbai, India) and L929 and HeLa cell lines were procured from the National Center of Cell Science (NCCS, Pune, India). Milli-Q water (18.2 MΩ cm) was used throughout the experiments.

2.2 Synthesis procedure for MMNs

In a typical synthesis procedure, $FeCl_3 \cdot 6H_2O$ (3.7 mM, 1 g) and $MgCl_2 \cdot 6H_2O$ (1.9 mM, 0.38 g) in a molar ratio of 2 : 1, PEG-diacid (3.5 g, 600 g per mole), and sodium acetate (NaAc, CH_3COONa, 3 g) were dissolved in 15 mL of EG in a 100 mL three neck round bottom flask. The mixture was heated to 180 °C in an inert (N_2 gas) environment for 30 min. A solution of sodium borohydride (0.05 g in 10 mL of EG) was prepared and injected into the reaction vessel at 180 °C. It was then refluxed for 8 h at 200 °C. The solution was cooled down to room temperature in an inert protected environment and the black precipitates were obtained by repeatedly washing with ethanol and Milli-Q water using a magnetic separation method.

2.3 Characterization techniques

The identification and purity of the phase were determined by X-ray diffraction (XRD) using a Philips powder diffractometer (PW3040/60) with Cu Kα radiation ($\lambda = 1.5405$ Å) and a Ni filter. The average crystallite size was calculated using the Scherrer relationship. Fourier transform infrared spectra of the dried powder samples were recorded using an FTIR instrument (Magna550, Nicolet Instruments Corporation, USA) using the KBr pellet technique. Thermal analysis was carried out in a thermo gravimetric–differential thermal analysis instrument (SDT Q100, USA). The samples under examination were heated from room temperature to 650 °C at a rate of 10 °C min^{-1} in a nitrogen atmosphere. The specific surface area, pore volume and pore size distribution of the MMNs were measured using a Micromeritics instrument (ASAP 2020). Prior to measurement, the sample was degassed at 120 °C for 6 h. The microstructure and surface morphology of the samples were analysed using a

transmission electron microscope (TEM, JEOL JEM-2100F) and field emission scanning electron microscope (FEGSEM, JEOL JEM-7600F). The composition of the sample was determined by the energy dispersive X-ray spectroscopy (EDX) technique. Weight chemical analysis was performed using an inductively coupled plasma-atomic emission spectrometer (ICP-AES, ARCOS, and Germany). Magnetic properties of the samples were measured in a Quantum design magnetic properties measurement system (PPMS).

2.4 *In vitro* DOX loading and release

DOX–MMN conjugates were prepared using electrostatic interactions between positively charged doxorubicin (DOX) and the negatively charged MMNs. The maximum loading amount of DOX into the pores of the MMNs was determined by the serial addition of MMNs (10, 50, 100, 150, 200, and 300 μg mL^{-1}) to a fixed concentration of DOX solution (16 μg mL^{-1} in 600 μL of PBS, pH 7.4) and the fluorescence was monitored at excitation with 480 nm, and the emission was recorded in the range 500–750 nm using a Hitachi F 2500 spectrofluorometer. To examine the loading efficiency, a standard curve was plotted with known concentrations of DOX dissolved in PBS at pH 7.4. The amount of DOX loaded (D_{Loaded}) into the nanoparticles was calculated as follows:

$$D_{loaded} = D_{total} - D_{supernatant} \quad (1)$$

where, D_{total} is the amount of drug added for loading and $D_{supernatant}$ is the amount of drug calculated from the supernatant after the settling of the MMNs by an external magnet. Furthermore, the loading efficiency of DOX into the MMNs was calculated using following equation:

$$\% \text{ efficiency} = \frac{D_{loaded}}{D_{total}} \times 100 \quad (2)$$

The *in vitro* drug release profile of the DOX–MMNs was determined by loading DOX–MMNs (5 mg) samples into a dialysis bag (Himedia, dialysis membrane-150, LA401), which was submerged in 5 mL of phosphate-buffered saline (PBS, pH = 7.4) and acetate buffer of pH 5.2 at 37 °C. The dialysate was taken out after a specific time interval to estimate the amount of drug released while the same amount of fresh buffer of the respective pH was added and kept in the shaker for further experimentation. The DOX concentration in the sample was measured by fluorescence intensity at $\lambda_{excitation}$ = 480 nm and $\lambda_{emission}$ in the range 500–750 nm using a Hitachi F 2500 spectrofluorometer.

2.5 Cell culture

The cell culture experiments were carried out with L929 and HeLa cell lines. L929 cells were grown in DMEM medium (Himedia Laboratories Pvt Ltd, Mumbai, India) and HeLa cells were grown in DMEM medium supplemented with 10% fetal bovine serum and an antibiotic–antimycotic mix (Himedia Laboratories Pvt Ltd, Mumbai, India) at 37 °C in a humidified and 5% CO_2 atmosphere (InCu-safe).

2.6 Rhodamine-6G–MMNs uptake by HeLa cells

Uptake of MMNs by HeLa cells was studied using confocal microscopy. MMNs were labelled with a positively charged fluorescent dye, rhodamine-6G by incubating MMNs (2 mg mL^{-1} in PBS, pH 7.4) with rhodamine-6G (1 μg mL^{-1}) with constant shaking for 12 h at room temperature. HeLa cells were plated on coverslips at a density of 1×10^5 cells per well in a 12-well plate. After 24 h, the cells were incubated with 0.1 mg mL^{-1} rhodamine-labeled MMNs for 4 and 24 h. The cells were washed 3 times with PBS (pH 7.4), fixed with 4% paraformaldehyde, mounted on a glass slide and then examined with an IX81 FV500 laser scanning confocal microscope (Olympus, Tokyo, Japan). The images were digitally magnified 6 times using FluoView software (Olympus, Tokyo, Japan).

2.7 *In vitro* biocompatibility of MMNs

The biocompatibility of MMNs was evaluated for L929 cells by using an MTS proliferation assay kit (Promega). For cytotoxicity assays, L929 cells were cultured (2×10^4 cells per well) in 96-well plates for 24 h. After incubation, the old media was replaced by fresh media containing bare MMNs in the concentration range 0.05 to 0.6 mg mL^{-1} and again incubated for another 24 and 48 h. After incubation, the old media was removed and 20 μL of MTS/PMS solution in 100 μL of DMEM media was added to each well. The plate was then incubated for 3 h and the absorbance at 490 nm was measured using a micro plate reader (Perkin Elmer 1420). The formazan dye generated by the live cells was proportional to the number of live cells. Cells without nanoparticles were considered as a control. The results were quantified by manually subtracting the blank value from each value then normalizing against the control.

2.8 *In vitro* antitumour efficacy of DOX–MMNs

HeLa cells were used to examine the *in vitro* antitumour efficacy of DOX–MMNs. Briefly, 2×10^4 cells per well were seeded in 96-well plate. After incubation for 24 h, different concentrations of DOX–MMNs (10 to 120 μg mL^{-1}) were added in five replicates. HeLa cells cultured in the absence of DOX–MMNs acted as controls. After being cultured for 24 and 48 h, the viability of the HeLa cells was determined using the MTS assay as described above. The IC_{50} values of the DOX–MMNs were expressed as the free DOX concentrations (1 to 7 μg mL^{-1}). The results were quantified by subtracting the blank value from each value and then normalizing against the control.

2.9 Subcellular localization study of DOX–MMNs

1×10^5 HeLa cells were seeded on a coverslip. After 24 h, the cells were treated with 0.1 mg mL^{-1} DOX–MMNs for 4 h followed by incubation for 30 min with 1 μM of Lysotracker Red DND-99 (Invitrogen). The cells were then fixed in 4% paraformaldehyde, and the nuclei were stained with DAPI (Calbiochem) for 10 min. Three-channel, optical images (DAPI, DOX, and Lysotracker Red) were collected using the sequential scanning mode (405, 480, and 543 nm excitation; 450, 560, and

595 nm emission) of an IX81 FV500 laser scanning confocal microscope (Olympus, Tokyo, Japan).

2.10 Cell morphological assessment of apoptosis

To detect morphological evidence of apoptosis, the cell nuclei were visualized following DNA staining with the fluorescent nuclear dye, ethidium bromide (EtBr). Briefly, cells were seeded at a concentration of 1×10^5 cells per well on the coverslip in 12-well tissue culture plates and treated with DOX–MMNs (0.1 mg of MMNs per mL, ~20 μg equivalent DOX per mL) for 4, 24 and 48 h. At the end of the incubation, the cells were washed thoroughly with PBS, fixed with 70% ethanol and incubated with EtBr (12 μM) for 10 min. The cells were again washed with PBS, mounted on a glass slide and then examined with an IX81 FV500 laser scanning confocal microscope.

2.11 *In vitro* magnetic hyperthermia experiments

The heating ability of the MMN suspension in PBS was obtained from time dependent calorimetric measurements using an induction heating unit (Comdel CLF-5000, Ameritherm) operating at frequency of 425 kHz. In brief, 0.5 mg of MMNs per mL (approximate metal ion concentration) in PBS was subjected to AC magnetic fields (AMFs) of 7 kA m^{-1} and 10 kA m^{-1}, at a frequency of 425 kHz, to evaluate the specific absorption rate (SAR). The SAR was calculated using the following equation:

$$\mathrm{SAR} = C\frac{\Delta T}{\Delta t}\frac{1}{m_{\mathrm{Fe}}} \quad (3)$$

where C is the specific heat of the solvent ($C_{\mathrm{water}} = 4.18\ \mathrm{J\ g^{-1}\ ^\circ C}$), $\Delta T/\Delta t$ is the initial slope of the time-dependent temperature curve and m_{Fe} is the mass fraction of Fe in PBS.

For the *in vitro* magnetic hyperthermia treatment (MHT) experiments, HeLa cells were grown up to 90% confluency in a 25 cm^2 culture flask. The culture medium was replaced with 2 mL of PEGylated MMNs dispersed in DMEM media at a concentration of 0.5 mg of MMNs per mL. After 24 h, the DMEM medium was removed and the cell layer was washed three times with PBS, detached from the substratum and pelleted by centrifugation. The cellular pellet was then transferred to a 2 mL Teflon sample vial, yielding concentrations of 2×10^6 HeLa cells per 1 mL of PBS. The cells were finally exposed to a magnetic hyperthermia setup, by applying an alternating magnetic field at a frequency of 425 kHz and at a magnetic field amplitude of 7 kA m^{-1} for 5 min to raise the temperature to 43–45 °C. The same procedure was also performed for DOX–MMNs to evaluate their combined effect for cancer cell death. For a comparative study, HeLa cells were treated using MHT alone (without MMNs and DOX) and, DOX–MMNs (0.5 mg mL^{-1}, 20 μg equivalent DOX per mL) with and without MHT. Cells without any treatment were used as a control. After the thermal treatment, the HeLa cells were centrifuged and settled with a magnet. The cell pellet was washed three times with PBS. Then, 100 μL of a 2×10^6 cells per mL solution was seeded in 96 well plates in 16 replicates, followed by incubation for 24 h in a 5% CO_2 incubator. The morphological features of the treated cells were observed by actin staining with phalloidin-tetramethylrhodamine-B-isothiocyanate and the nucleus by 4,6-diamidino-2-phenylindole (DAPI) according to the protocol of Sigma-Aldrich. 3-(4,5-Dimethyl-thiazol-2yl)-2,5-diphenyl tetrazolium bromide (MTT) as well as a live/dead assay were used for cell viability studies. For the MTT assay, the cell culture supernatant was replaced with 100 mL of fresh medium containing 10 μL of 5 mg mL^{-1} MTT. The plates were then incubated for 4 h at 37 °C. The purple formazan crystals were dissolved in 50% DMF in a water solution containing 5% SDS (sodium dodecyl sulfate). Thereafter, the absorbance was measured at a wavelength of 550 nm in a plate reader.

The cell viability percentage was calculated using the following equation:

$$\text{Cell viability} = \frac{\text{Absorbance of the treated well with MMNs}}{\text{Absorbance of control}} \times 100 \quad (4)$$

For the live/dead assay, the treated cells were stained with calcein AM (2 μM) and ethidium homodimer-1 (4 μM) for 30 min. The cells were observed using an IX81 FV500 laser scanning confocal microscope (Olympus, Tokyo, Japan).

3 Results and discussion

3.1 Structural characterization of MMNs

The microstructure and surface morphology of the as-synthesized MMNs were observed by SEM (Fig. 1a and b) and TEM (see ESI, Fig. S1a–c†). The microstructures show that the particles are spherical and porous. The submicron sized (>250 nm) nanoassemblies were formed in the absence of an external reducing agent but a reduction in the size of nanoassemblies (<100 nm) was obtained in the presence of an extra reducing agent, sodium borohydride ($NaBH_4$). The addition of a strong reducing agent during the reaction initiated a super saturation state that led to the formation of a large number of nuclei and subsequent assembling resulted in the evolution of smaller MMNs.[20] The XRD pattern of the MMNs shows a typical face centered cubic inverse spinel structure (Fig. S2a†). The crystallite size estimated from the peak broadening corresponding to the (311) plane using the Debye–Scherrer equation was found to be ~11.5 nm.

A lattice parameter of 8.32 Å and a unit cell volume of 577 $Å^3$ were obtained. A comparison of the crystallite size (estimated from XRD) and the cluster size from high resolution TEM images indicates that the MMNs consisted of an assembly of individual

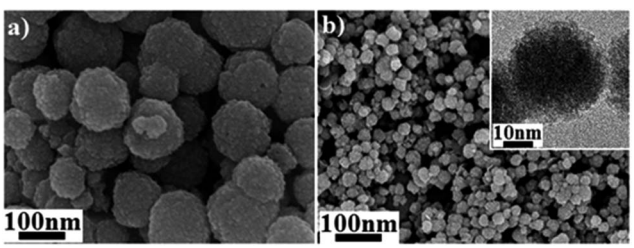

Fig. 1 SEM images of PEGylated MMNs synthesized (a) without and (b) with $NaBH_4$ (0.05 g). The inset shows the TEM image of a single MMN.

particles with sizes of less than 12 nm. EDX analysis confirms the composition of the MMNs (Fig. S2b†). The formation mechanism of the MMNs can be described as a two stage reaction. The nucleation of nanocrystals occurs in the primary stage of the reaction in a supersaturated solution followed by aggregation into larger aggregates or secondary particles.[12,21] The number density of the particles as well as the relative strength of the anisotropic dipole–dipole and isotropic van der Waals coupling also influence the above mechanism.[22] The nitrogen (N_2) adsorption–desorption isotherm shows a pore size distribution having intrapores (~3 nm) and interpores (~30 nm) and a specific surface area of 92 $cm^2\ g^{-1}$ (Fig. 2a). The mesoporous nature, size of below 100 nm and large specific surface area make MMNs ideal nanocarriers for drug delivery applications. The Fourier-transform infrared (FTIR) spectrum (Fig. 2b) of PEGylated MMNs shows the presence of bands at 1107 and 1402 cm^{-1} which are due to the C–O–C ether stretching vibration of HOOC–PEG–COOH with bands shifted compared to those of the free PEG molecule indicating its attachment on the MMNs.[23]

The bands at 1608 and 3400 cm^{-1} are due to the O–H bending and stretching frequencies of the carboxylate group which are different and at a lower wavenumber than the free O–H group indicating the presence of a hydrogen bond in the EG molecule and its attachment on the surface of the MMNs.[23] The thermogravimetry (TG) analysis (Fig. S3a†) shows the sequential weight loss in different temperature ranges due to the loss of physically adsorbed and chemically bonded water molecules and the decomposition of organic carbonaceous materials to form CO_2 gas. The TG analysis along with the FTIR data confirms the attachment of PEG-diacid on the MMNs. Furthermore, the zeta potential of the MMNs was determined and found to be ~−23.6 mV. The coating of PEG-diacid enables a good colloidal stability of the MMNs in PBS, which is necessary for their use in drug delivery applications (Fig. S3b†). The *M–H* curve (Fig. S4†) shows a typical superparamagnetic nature of the MMNs with magnetization of 57 emu g^{-1} measured in a field of 2 Tesla. The blocking temperature (T_b) was found to be 100 K from the zero field cool and field cool (ZFC–FC) curve. The higher magnetic moment and superparamagnetic nature of the MMNs are the required attributes for magnetic hyperthermia (MHT).

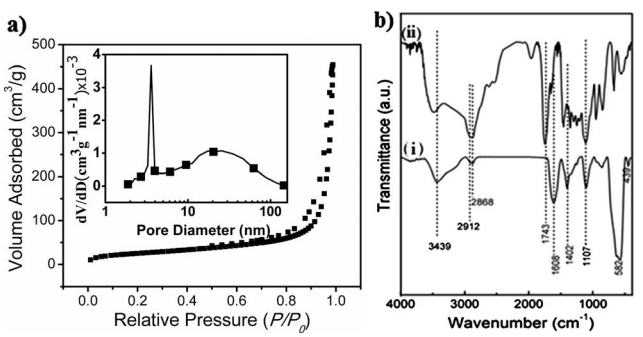

Fig. 2 (a) N_2 adsorption–desorption isotherms and pore size distribution (inset) of as-synthesized MMNs. (b) FT-IR spectra of the (i) PEG-diacid coated MMNs and (ii) bare PEG-diacid.

3.2 *In vitro* and intracellular DOX release

We have further demonstrated the interaction and cellular uptake of rhodamine-6G (λ_{ex} = 530 nm, λ_{em} = 555 nm) labelled MMNs by cancer cells. Fig. 3i–iii shows the appearance of granulated red fluorescence after incubation for 4 h, which indicates the uptake of MMNs by the HeLa cells. The higher uptake of MMNs may be attributed due to the PEG coating, which retards the adsorption of unwanted biomolecules on the surface.[16]

The biocompatibility of MMNs was studied on mouse fibroblast cells (L929) by MTS assay. We observed no significant cytotoxicity effect of the MMNs on the cells at concentrations of up to 0.4 mg of MMNs per mL (in terms of the metal ion concentration) after 24 and 48 h of incubation (Fig. S5a and b†). Microscopic images show that up to 0.2 mg of MMNs per mL, the growth and morphology of the L929 cells are similar to cells incubated in media without MMNs (control) at the corresponding time intervals. However, at a concentration of 0.6 mg of MMNs per mL, a slight shrinkage of the cells was observed without affecting the viability of the cells. The cationic DOX was used as a model anticancer drug for loading and release studies of the MMNs. The DOX was loaded through electrostatic interaction with the negatively charged carboxyl enriched MMNs in PBS medium (pH = 7.4) by mixing for 24 h. The fluorescence intensity of supernatant liquid was recorded after magnetic separation of DOX-bound MMNs. The fluorescence intensity of the free DOX (16 μg in 600 μL of PBS) quantified by UV-vis absorbance with a prominent DOX peak at 490 nm, decreased upon the addition of different amounts of MMNs (Fig. 4a). This is obvious due to the quenching of the DOX fluorescence upon interaction with the MMNs. 80% (w/w) drug loading was achieved under physiological conditions (pH 7.4) in which the daunosamine group of DOX was deprotonated and its solubility in water decreased.[24] The large amount of DOX loading could possibly be due to the high specific surface area, negative charge and mesoporous nature of the MMNs.

Next, we investigated the release profile of DOX at different physiological pH values. A higher release (75–80%) was observed at a lower pH (5.2) as compared to 20–25% at a higher pH (7.4) within 24 h (Fig. 4b). The high release of DOX in a mild acidic environment might be due to the dissolution of PEG and weakening of electrostatic bonding by excessive deprotonation of the daunosamine group of the DOX.[6,23] This is favourable for

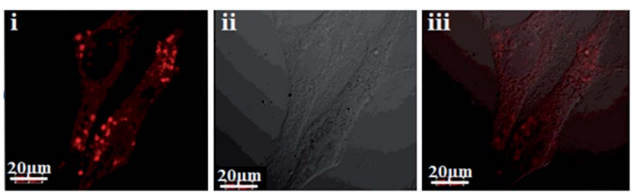

Fig. 3 Cellular uptake behaviour of rhodamine-6G labelled MMNs by HeLa cells after incubation for 4 h: confocal image of (i) rhodamine-6G labeled MMNs, (ii) differential interference contrast (DIC) image, (iii) overlay image of (i) and (ii) showing red granulated fluorescence which confirms the presence of MMNs inside the cancer cells.

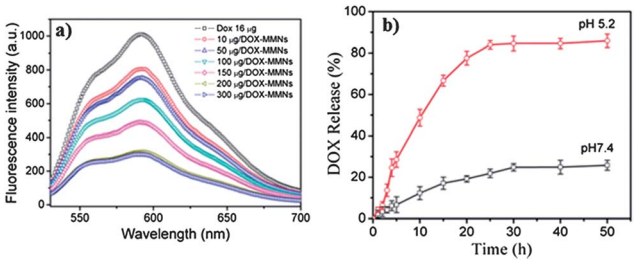

Fig. 4 (a) Fluorescence spectra of DOX solution (16 μg in 600 μL of PBS, pH 7.4) with different concentrations of MMNs (in terms of the metal concentration) for the preparation of DOX–MMNs and (b) release profile of DOX from MMN solution at pH 5.2 and pH 7.4. The measurements were made at 37 °C.

the effective treatment of cancer because the majority of tumours have mildly acidic cellular environments.[24,25] Additionally, the mesoporous nature of the MMNs protects the drug payload from unwanted enzymatic degradation and protein biofouling which usually happens with free DOX in blood.[24]

Next, we tested the antitumour ability of DOX–MMNs on HeLa cells. The temporal concentration response of the DOX–MMN conjugates was monitored by the MTS assay (Fig. S6a and b†). The IC_{50} values for the conjugate were found to be 3.5 and 1 μg of DOX per mL at 24 and 48 h, respectively. Having established an antitumour activity of the DOX–MMN conjugates, we studied *in vitro* DOX release by the conjugates in HeLa cancer cells, observed through confocal fluorescence imaging (Fig. 5a and b). The morphology of the HeLa cells was observed by incubating them with the conjugates (0.1 mg of MMNs per mL, ~20 μg equivalent DOX per mL) for 4, 24 and 48 h (Fig. 5b-v–vii) and the results were compared with the free DOX (~20 μg mL^{-1}) treated cells (Fig. 5b-ii–iv). Cells cultured under the same conditions without DOX–MMNs incubation were used as a control (Fig. 5b-i). After entering into the cells, the DOX was released from the conjugates in a mildly acidic environment of late endosomes/lysosomes (~pH 4.7) due to deprotonation of the daunosamine group of DOX (Fig. 5a). Lysotracker red was used to stain the DOX–MMNs encapsulated lysosomes, which is more evident due to the appearance of an orange colour due to the overlay of green (DOX) and red (lysotracker) florescence as shown in (Fig. 5a-i–iv). After uptake for 4 h, DOX started to diffuse from the cellular compartment to the nuclear compartment. Several reports show that DOX directly intercalates with DNA or DNA topoisomerase II and inhibits RNA synthesis to elicit its cytotoxic effect.[25,26] Interestingly, we observed a good relationship between the antitumour activity of the DOX–MMNs and the stimulation of apoptosis. The apoptotic nuclei were observed by staining them with a nuclear dye ethidium bromide that gave red fluorescence when excited at 518 nm. The DOX–MMNs gave green fluorescence due to the presence of DOX. Fig. 5b-i shows that cells from the control group exhibited evenly stained nuclei and intact nuclear membranes showing 99% cell viability. In contrast to this, Fig. 5b-ii–iv (DOX alone) and Fig. 5b-v–vii (DOX–MMN conjugates) show loss of cell membrane integrity, complete DNA fragmentation and a reduction in the size of the nucleus. These are the most prominent morphological markers used for the

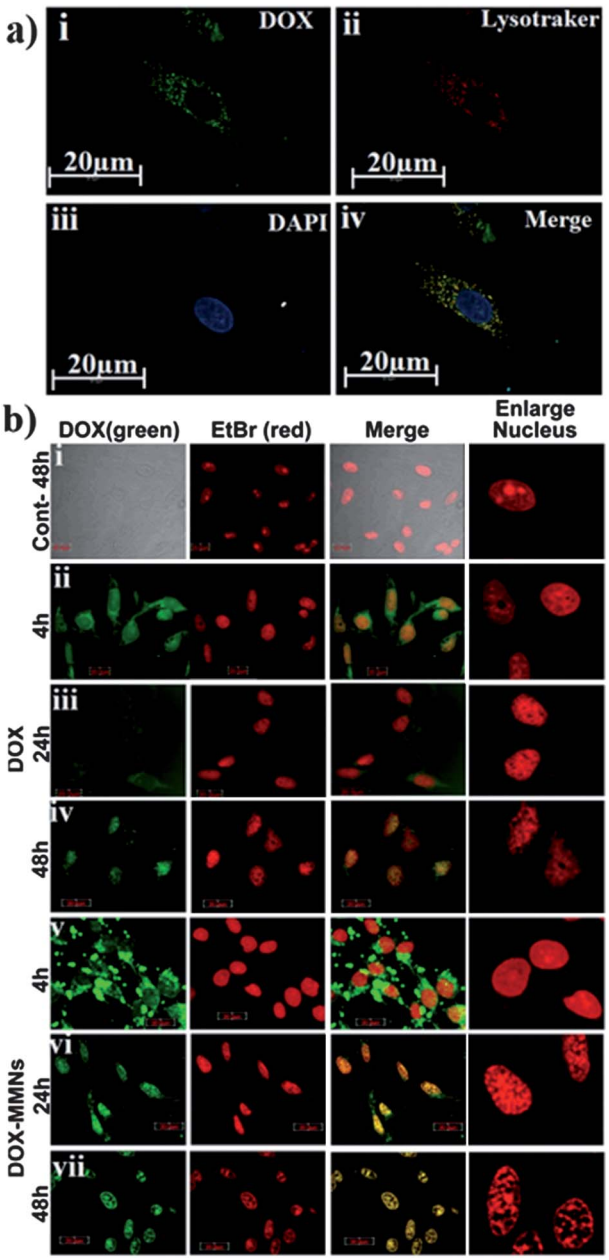

Fig. 5 (a) Subcellular localization of DOX–MMNs in HeLa cells after incubation for 4 h: (a-i) DOX–MMNs (fluorescence of DOX, green color), (a-ii) lysosomal compartment of cells (lysotracker dye, red), (a-iii) nucleus stained with DAPI (4,6-diamidino-2-phenylindole, blue color), (a-iv) merged image of DOX–MMNs and lysotracker signals (orange colour) suggest localization of DOX–MMNs in the lysosomal compartment (pH 5) of the cell. (b) *In vitro* efficacy of DOX–MMNs for the delivery of DOX in cancer cells. Confocal laser scanning microscopy (CLSM) images show the apoptosis (DNA fragmentation) in HeLa cells. (i) Control (without DOX) showing rounded, intact nucleus; (ii–iv) with DOX (20 μg mL^{-1}) alone and (v–vii) with DOX–MMN conjugates (~0.5 mg of MMNs per mL in terms of the metal ion concentration with ~20 μg equivalent DOX per mL) at indicated time intervals of 4, 24, and 48 h at 37 °C, without any heat treatment. The green fluorescence shows DOX–MMNs, red fluorescence shows ethidium bromide (EtBr) stained nuclei. The scale bar is 50 μm. Enlarged images show typical apoptotic nuclei with fragmented morphology.

identification of apoptosis in cancer cells and represent important events in successful chemotherapeutic treatment from which a cancer cell cannot return to a live condition. Gao *et al.*

have demonstrated the same approach of apoptosis induction in MCF-7 and drug-resistant MCF-7/ADR breast cancer cells using DOX released from mesoporous silica nanoparticles.[25] Likewise, Li and co-workers reported DNA fragmentation as a major event in the apoptosis of HeLa cells using DOX loaded dextran nanoparticles.[26] Our results show that DOX–MMN conjugates have toxic effects comparable to those of the free DOX, although free DOX induces more cell death. The free DOX enters into the cytoplasm of the cancer cells through passive diffusion but is easily effluxed by the P-glycoprotein efflux pump, active in all types of tumour,[25,27] whereas DOX–MMN conjugates are internalized *via* endocytosis.[24,25] Drug efflux by the cancer cell is a major hurdle for effective chemotherapeutic treatment. These conjugates not only have the capability to reduce the toxicity of free DOX but also help in enhancing the therapeutic efficacy of DOX by reducing the drug efflux problem and increasing the DOX retention time inside cancer cells.

3.3 *In vitro* chemo-thermal evaluation of DOX–MMNs

Previous studies have reported the extensive use of $MgFe_2O_4$ nanoparticles for magnetic hyperthermia.[28,29] In order to use DOX–MMNs for chemo-thermal therapy, the heating efficiency of MMNs was evaluated under an AMF with a frequency of 425 kHz and strengths of 7 and 10 kA m^{-1} s^{-1} (Fig. 6a). The temperature of the solution containing 0.5 mg of MMNs per mL of PBS increased to 42–43 °C within 5 minutes. This temperature is recommended as the therapeutic threshold temperature required for hyperthermia. We found a variation of the SAR value at the two different field strengths, 7 kA m^{-1} s^{-1} (95.38 W per g of Fe) and 10 kA m^{-1} s^{-1} (153.4 W per g of Fe) at a fixed frequency of 425 kHz. This is obvious because the SAR value increased proportionally to the field strength and frequency.[9,30]

Next, we investigated the rationale behind the hyperthermia induced enhancement of the DOX toxicity. The bare MMNs and DOX–MMN conjugates (~20 μg equivalent DOX per mL) at concentrations of 0.5 mg of MMNs per mL were incubated for 24 h with cancer cells. The cells without MMNs and DOX treatment were used as a control. After incubation for 24 h, the cells (2×10^6 cells per pellet) were subjected to an AMF of 7 kA m^{-1} s^{-1} at a frequency of 425 kHz for 5 minutes to evaluate the individual and combined effect of bare MMNs and DOX–MMN conjugates on the proliferation of cancer cells. Following magnetic hyperthermia treatment, the cells were washed with PBS and allowed to grow for 24 h. The morphology of the control and MHT treated cells were observed by DIC and confocal imaging (Fig. 6bi–iv). The actin filaments were stained with phalloidin-tetramethylrhodamine-B-isothiocyanate and the nucleus with 4,6-diamidino-2-phenylindole dye (DAPI). The confocal images show plasma membrane distortion, blebbing, disorganization of the cytoskeleton protein (F-actin) and shrinkage of the nucleus upon treatment, a prominent marker of hyperthermia induced late apoptosis in cancer cells (Fig. 6ii and iv). Thomas *et al.* also found a similar apoptosis phenomenon when breast cancer cells (MDA-MB-231) were subjected to MHT with magnetic core silica nanoparticles (MCSNs).[4] A similar approach was attempted by Prasad *et al.* using γ-$Mn_xFe_{2-x}O_3$ for the hyperthermia treatment of cancer cells.[31]

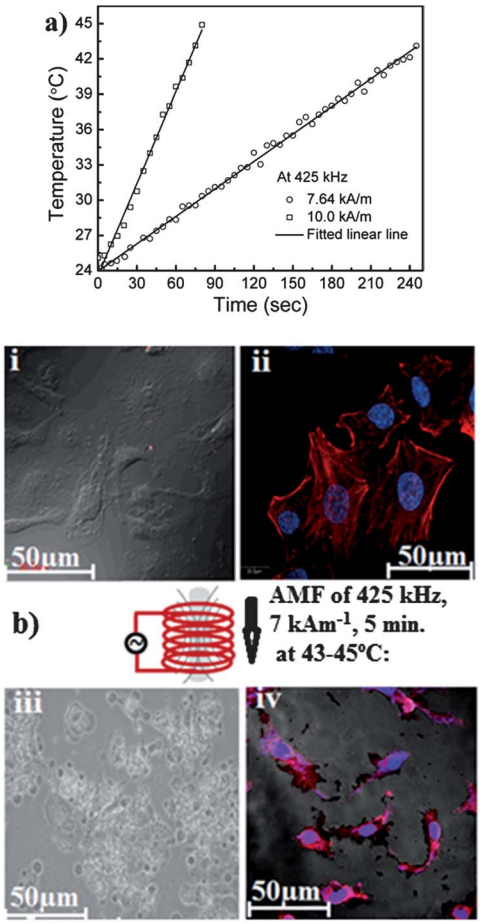

Fig. 6 (a) Temperature *vs.* time plots of PEGylated MMNs (5 mL, 0.5 mg of MMNs per mL in PBS in terms of the metal concentration) under AC magnetic fields of different strengths. (b) *In vitro* hyperthermia (MHT) study of MMNs alone with HeLa cells under an AC magnetic field (AMF) of 425 kHz, 7 kA m^{-1} for 5 minutes at 43–45 °C: (b-i) differential interference contrast (DIC) image, (b-ii) confocal image of control HeLa cells stained with phalloidin-tetramethylrhodamine-B-isothiocyanate (red) for actin filaments and 4,6-diamidino-2-phenylindole dye (DAPI, blue color) for the nucleus, (b-iii and iv) DIC and confocal images of MHT treated HeLa cells showing the blebbing formation and distortion of the cell membrane, a morphological indication of cell late apoptosis/necrosis.

The live/dead assay was performed for a qualitative assessment of the dual therapy effect on the viability of cancer cells (Fig. 7a). A quantitative estimation of cell viability was achieved using the MTT assay (Fig. 7b). Both the live/dead and MTT assay demonstrated a significant increase in toxicity of the DOX–MMNs, when combined with MHT (Fig. 7a and b). It was observed that cells treated with MMNs and exposed to MHT showed 45% cell death while cells treated with DOX–MMN conjugates (~20 μg equivalent DOX per mL) without MHT exhibited 65% cell death. However, cells simultaneously treated with DOX–MMN conjugates (~20 μg equivalent DOX per mL) and MHT resulted in cell death of up to 90%. Our results are consistent with the findings of Brule *et al.*, which demonstrated the combined effect of chemo-thermal therapy on cancer cells using magnetic alginate microspheres. Their study showed that the combination of a drug and magnetic hyperthermia induces more cell death as compared to the effects of individual

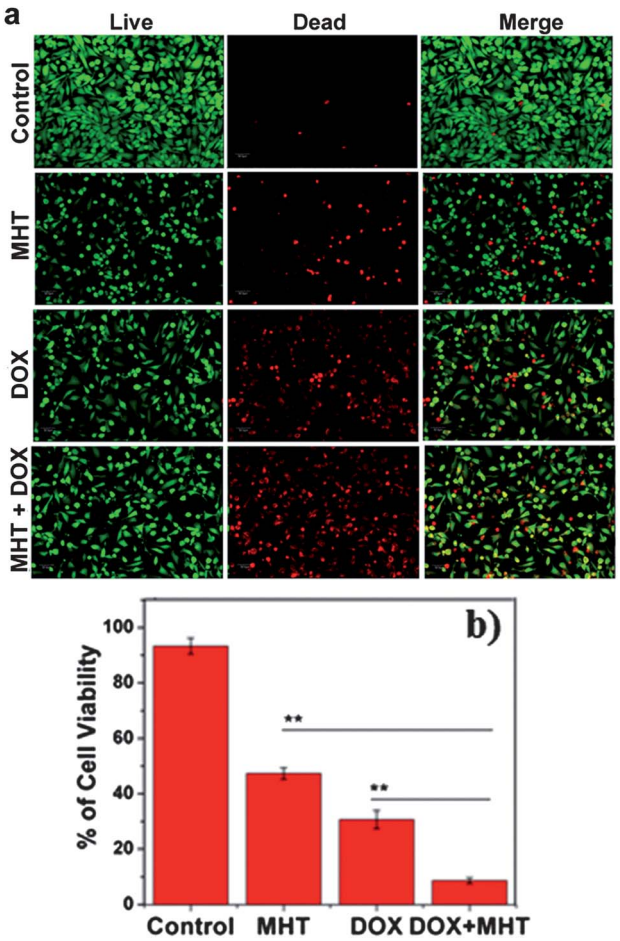

Fig. 7 (a) Live/dead assay for the synergistic effect of chemo-thermal therapy *in vitro*: cells were stained with calcein (green) and ethidium homodimer-1 (red) for the visualization of live and dead cells, respectively. (b) Cells were treated with free DOX (~20 μg mL^{-1}), MMNs, and DOX–MMN conjugates (~20 μg equivalent DOX per mL). The cells without DOX and MMN incubation were used as a control. Quantitative evaluation of cell viability was determined using the MTT assay. The DOX–MMN efficacy was significantly enhanced when combined with hyperthermia (MHT), almost 90% of cancer cells died. The viability of the control cells or DOX incubated cells was not effected by hyperthermia. Data shown are means ± SD from $n = 3$. $^{**}P < 0.01$.

therapy.[3] A similar result was reported by Lee *et al.* in their study with lung cancer cells in which they showed that hyperthermia improves the efficacy of chemotherapy using mesoporous silica nanoparticles.[32] On similar lines, the present study also suggests that the combination of chemo-thermal therapy induces the destruction of HeLa cancer cells more efficiently than the individual effect of DOX or MHT treatment alone. Noh *et al.* even reported the significance of the dual therapy by inducing more cell death in the drug resistant cancer cell line DLD-1-ADR *vs.* normal cancer cells.[33] With the same views as in the studies by Noh *et al.*, it is predicted that the problem of drug resistant cancer cells and drug efflux, a major hurdle in the treatment of cancer, can be solved by the application of chemo-thermal therapy. With these features, MMNs appear to be a potential integrated nanoparticles system combining magnetic hyperthermia with drug delivery for effective cancer therapy.

4 Conclusions

In summary, biocompatible and biodegradable PEG coated carboxyl-enriched $MgFe_2O_4$ MMNs with sizes less than 100 nm have been developed to evaluate the synergistic effect of chemo-thermal therapy *in vitro*. The negatively charged, mesoporous MMNs help in terms of a high loading efficiency and pH induced DOX release for cancer cell death. Hyperthermia significantly enhances the therapeutic efficacy of DOX, leading to more cell death in comparison to the individual treatments of hyperthermia or DOX. This study suggests that MMNs act as a novel therapeutic mediator, having the potential to reduce the toxicity of DOX and increase its aqueous solubility with two therapeutic modalities, chemo- and thermal therapy in a single system, for the effective treatment of cancer. Further studies are ongoing for the development of DOX–MMN conjugation through acid labile hydrazone bonds and their implication in bimodal drug delivery and MR imaging. Additionally, the role of Mg^{2+} ions in the apoptosis of cancer cells is under examination.

Acknowledgements

The study is supported by Nanomission, Department of Science and Technology (DST) and Nanotechnology Section, Department of Information Technology (DIT), Govt of India. We thank Asif S. Khan for his assistance with the hyperthermia experiment. The authors are also thankful to the Centre for Research in Nanotechnology and Science (CRNTS), I. I. T. Bombay.

Notes and references

1 R. A. Petros and J. M. Desimone, *Nat. Rev. Drug Discovery*, 2010, **9**, 615–627.
2 S. Chandra, K. C. Barick and D. Bahadur, *Adv. Drug Delivery Rev.*, 2011, **63**, 1267–1281.
3 S. Brule, M. Levy, C. Wilhelm, D. Letourneur, F. Gazeau, C. Menager and C. L. Visage, *Adv. Mater.*, 2011, **23**, 787–790.
4 C. R. Thomas, D. P. Ferris, J. H. Lee, E. Choi, M. H. Cho, E. S. Kim, J. F. Stoddart, J. S. Shin, J. Cheon and J. I. Zink, *J. Am. Chem. Soc.*, 2010, **132**, 10623–10625.
5 J. You, R. Zhang, G. Zhang, M. Zhong, Y. Liu, C. S. V. Pelt, D. Liang, W. Wei, A. K. Sood and C. Li, *ACS Nano*, 2012, **158**, 319–328.
6 S. P. Sherlock, S. M. Tabakman, L. Xie and H. Die, *ACS Nano*, 2011, **5**, 1505–1512.
7 K. Yang, S. Zhang, G. Zhang, X. Sun, S. T. Lee and Z. Liu, *Nano Lett.*, 2010, **10**, 3318–3323.
8 P. Pradhan, J. Giri, F. Rieken, C. Koch, O. Mykhaylyk, M. Doblinger, D. Bahadur and C. Plank, *J. Controlled Release*, 2010, **142**, 108–121.
9 K. C. Barick, M. Aslam, Y. P. Lin, D. Bahadur, P. V. Prasad and V. P. Dravid, *J. Mater. Chem.*, 2009, **19**, 7023–7029.
10 J. T. Jang, H. Nah, J. H. Lee, S. H. Lee, S. H. Moon, M. G. Kim and J. Cheon, *Angew. Chem., Int. Ed.*, 2009, **48**, 1234–1238.
11 K. C. Barick, S. Singh, N. V. Jadhav, D. Bahadur, B. N. Pandey and P. A. Hassan, *Adv. Funct. Mater.*, 2012, **22**, 4975–4984.

12 B. Luo, S. Xu, A. Luo, W. R. Wang, S. L. Wang, J. Guo, Y. Lin, D. Zhao and C. C. Wang, *ACS Nano*, 2011, **5**, 1428–1435.
13 B. Luo, S. Xu, W. F. Ma, W. R. Wang, S. L. Wang, J. Guo, W. L. Yang, J. H. Hu and C. C. Wang, *J. Mater. Chem.*, 2010, **20**, 7107–7113.
14 J. Ge, Y. Hu, M. Biasini, W. P. Beyermann and Y. Yin, *Angew. Chem., Int. Ed.*, 2007, **46**, 4342–4345.
15 J. Liu, Z. Sun, Y. Deng, Y. Zou, C. Li, X. Guo, L. Xiong, Y. Gao, F. Li and D. Zhao, *Angew. Chem., Int. Ed.*, 2009, **48**, 5875–5879.
16 Y. Zhang, N. Kohler and M. Zhang, *Biomaterials*, 2002, **23**, 1553–1561.
17 J. Xie, C. Xu, N. Kohler, Y. Hou and S. Sun, *Adv. Mater.*, 2007, **19**, 3163–3166.
18 C. Martinez-Boubeta, L. Balcells, R. Cristòfol, C. Sanfeliu, E. Rodríguez and R. Weissleder, *Nanomedicine: Nanotechnology, Biology, and Medicine*, 2010, **6**, 362–370.
19 K. Krishnamoorthy, J. Y. Moon, H. B. Hyun, S. K. Cho and S. J. Kim, *J. Mater. Chem.*, 2012, **22**, 24610–24617.
20 G. Cao, *Nanostructures and Nanomaterial's: Synthesis, Properties and Applications*, Imperial College Press, 2nd edn, 2004.
21 L. T. Su, A. I. Y. Tok and F. Y. C. Boey, *CrystEngComm*, 2009, **11**, 1880–1885.
22 A. Baskin, W. Y. Lo and P. Kral, *ACS Nano*, 2012, **6**, 6083–6090.
23 F. Hu, K. W. Macrenaris, E. A. Waters, E. A. S. Sikma, A. L. Eckermann and T. J. Meade, *Chem. Commun.*, 2010, **46**, 73–75.
24 Y. Tian, L. Bromberg, S. N. Lin, T. A. Hatton and K. C. Tam, *J. Controlled Release*, 2007, **121**, 137–145.
25 Y. Gao, Y. Chen, X. Ji, X. He, Q. Yin, Z. Zhang, J. Shi and Y. Li, *ACS Nano*, 2011, **5**, 9788–9798.
26 Y. L. Li, L. Zhu, Z. Liu, R. Cheng, F. Meng, J. H. Cui, S. J. Ji and Z. Zhong, *Angew. Chem., Int. Ed.*, 2009, **48**, 9914–9918.
27 F. M. Kievita, F. Y. Wang, C. Fang, H. Mok, K. Wang, J. R. Silberb, R. G. Ellenbogen and M. Zhang, *J. Controlled Release*, 2011, **152**, 76–83.
28 S. Yukumi and Y. Watanabe, *Int. J. Hyperthermia*, 2009, **25**, 416–421.
29 A. Chalkidou, K. Simeonidis, M. Angelakeris, T. Samaras, C. Martinez-Boubeta, L. Balcells, K. Papazisis, C. Dendrinou-Samara and O. Kalogirou, *J. Magn. Magn. Mater.*, 2011, **323**, 775–780.
30 L. Lartigue, P. Hugouneng, D. Alloyeau, S. P. Clarke, M. Levy, J. C. Bacri, R. Bazzi, D. F. Brougham, C. Wilhelm and F. Gazeau, *ACS Nano*, 2012, **6**, 10935–10949.
31 N. K. Prasad, K. Rathinamy, D. Panda and D. Bahadur, *J. Mater. Chem.*, 2007, **17**, 5042–5051.
32 H. Lee, S. Kim, B. Choi, M. Park, J. lee, S. Jeong, E. K. Choi, B. Lim, C. Kim and H. Park, *Int. J. Hyperthermia*, 2011, **27**, 698–707.
33 S. Noh, W. Na, J. Jang, J. Lee, E. J. Lee, S. H. Moon, Y. Lim, J. S. Shin and J. Cheon, *Nano Lett.*, 2012, **6**, 5266–5273.